

**Scanning force microscope induced growth and  
dissolution on single crystal gypsum ( $\text{CaHSO}_4 \cdot 2\text{H}_2\text{O}$ )**

**Benjamin Arthurs**

**Spring 2008**

**Dr. J. T. Dickinson**

**Department of Physics and Astronomy**

**College of Sciences**

**TO THE UNIVERSITY HONORS COLLEGE:**

**As thesis advisor for \_\_\_\_\_,**

**I have read this paper and find it satisfactory.**

\_\_\_\_\_  
**Thesis Advisor**

\_\_\_\_\_  
**Date**

## Précis

Repetitive structures dominate the microscopic landscape of our world. Despite the seemingly endless variety of living organisms, each shares a similar genetic blueprint in the form of DNA, a repetitive linear sequence composed of much smaller molecular building blocks called nucleotides. These blueprints guide the synthesis of proteins, the functional machinery of life, which also owe their properties to a sequential substructure of linked amino acids. Inorganic objects follow the same paradigm, where macroscopic properties depend on a highly ordered microscopic structure composed of repeating building blocks. Crystals, including diamond and table salt, are composed of atomic building blocks in highly organized three-dimensional lattices. Studying the atomic-scale properties of crystals is a challenging endeavor that can yield valuable knowledge about such materials and how they form.

The difficulty of studying the atomic substructure of crystalline substances is that their building blocks are far too small to observe with conventional microscopes. In order to “see” crystals at this level of detail researchers use more complicated methods such as bombarding materials with x-rays, electrons, and neutrons. Another method utilizes touch to “see” the surface of a crystal, similar to how one uses touch to visualize obstacles in a dark room. One such technique is known as scanning force microscopy (SFM). SFM touches a crystal with a needle-like probe only a few atoms wide, which is attached to the bottom of a reflective cantilever. When the probe tip is scanned about an area on a sample, it moves up and down as it encounters bumps and depressions. This movement bends the cantilever and changes the angle of a laser beam shone on its reflective surface. Light from the laser hits a detector, and the signal produced can be translated into a three dimensional image of the crystal surface. SFM is very

sensitive and does not lend itself well to studying rough objects, so crystals with extremely flat topographies including calcite, brushite, and gypsum are often used.

SFM is useful for observing how crystal surfaces change over time as they incorporate more atomic building blocks and grow, or lose material as they dissolve. More recently it became apparent that the SFM probe could also control growth and dissolution on samples of calcite and brushite. Growth was achieved by pressing the tip very lightly into the sample and scanning over shallow gauges in the surface. Dissolution occurred when the tip was pressed into the material with greater force. These phenomena provide useful information about the properties of calcite and brushite, as well as the means to manufacture extremely flat surfaces where no atomic gauges or bumps are present.

Applying similar techniques on gypsum is the next challenge. We hoped to affect growth and dissolution on its surface, thereby improving our knowledge about SFM induced surface remodeling and gypsum itself. Our results confirm that tip induced growth is possible on gypsum surfaces placed in highly concentrated solutions. The forces required turned out to be even lower than those used on brushite. We were also able to promote dissolution on exposed crystal edges. Surprisingly, we observed massive material loss extending away from the region of tip contact. This phenomenon appeared to be the result unstable surface features formed during tip induced dissolution. A relationship between dissolution rate and tip contact force was determined and matched relatively well with previously reported data for calcite and brushite. Finally, we implemented a new technique to create small pits on the gypsum surface by pressing the SFM tip into the surface at a single point. Our experiments captured information about the properties of gypsum, identified several phenomena worthy of future research, and exposed SFM techniques useful in the manufacture of novel nano-topographies and atomically flat surfaces.

## Table of Contents

I. Introduction	1
<i>a) Microscopic Features of the Natural World</i>	1
<i>b) The Study of Crystalline Solids</i>	2
<i>c) Scanning Force Microscopy</i>	5
<i>d) Crystal Growth and Dissolution Mechanisms</i>	7
<i>e) Applications of Scanning Force Microscopy</i>	9
<i>f) Properties of Gypsum</i>	11
II. Hypothesis	14
III. Methodology	14
IV. Results and Discussion	15
<i>a) Tip Induced Growth</i>	15
<i>b) Tip Induced Dissolution</i>	19
<i>c) Modeling Tip Induced Wear Track Formation</i>	24
<i>d) Pit Formation by Tip Indentation</i>	28
V. Conclusions	30
VI. Acknowledgements	31
VII. Appendix: Figures	32
<i>Figures 1-4</i>	32
<i>Figures 5-6</i>	33
<i>Figure 7</i>	34
<i>Figures 8-9</i>	35
<i>Figure 10</i>	36
<i>Figure 11-12</i>	37
<i>Figure 13</i>	38
VIII. References	39

## I. Introduction

### *a) Microscopic Features of the Natural World*

The macroscopic complexity of the natural world can appear daunting and apparently random. Life takes on a seemingly infinite number of forms and inert structures vary greatly. This variety, observed at larger length scales, is in sharp contrast to the commonalities shared amongst microscopic structures. At molecular and atomic length scales, nature does not permit the pliability observed macroscopically, but follows a more rigid paradigm where repetitive structures dominate the landscape. Here, fundamental chemical building blocks must be arranged in constrained arrays. Understanding the organization of such microscopic structures and the dynamics of how they form provide us the ability to predict and control their corresponding macroscopic properties.

Living organisms achieve much of their functionality due to the microscopic biopolymers within their cells. Despite the broad spectrum of living organisms, deoxyribonucleic acid (DNA) and proteins are common microscopic constituents, which are celebrated as the functional machinery of biology. DNA, often described as the blueprint for a given organism, is a repeating structure composed of only four varieties of nucleotide subunits. These molecular building blocks are connected in a linear array, whose sequence stores genetic information. Knowledge of nucleotide sequences, and the processes by which they are linked, has yielded impressive technologies for identifying and treating human genetic diseases. Proteins are also linear chains, whose repetitive building blocks are amino acids. They provide catalytic activity and structural support for cells. Understanding the dynamics of protein synthesis and degradation, and the amino acid sequences of many functional proteins, has led to countless advances in biomedical

science. Many of the macroscopic curiosities in the living world can be deciphered and manipulated by studying microscopic substructures including DNA and protein.

Functional properties of inorganic materials also result from the arrangement of their atomic building blocks. Crystalline solids are the most highly ordered examples. They are composed of atomic and molecular subunits arranged in a repeating three dimensional lattice. Each subunit is coordinated by its neighbors via electrical and chemical interactions. The physical properties resulting from this structure depend on the elemental composition of the crystal and the particular lattice geometry in which its subunits are constrained. Even subtle microscopic impurities and deviations in growth processes can have profound macroscopic effects on the material. Gypsum, a crystal of calcium sulfate dihydrate, appears in nature as transparent selenite, translucent satin spar or alabaster, and desert rose (see *Figure 1*).<sup>1</sup> These forms differ greatly in appearance, but share common microscopic structures that deviate only because of slight differences in the environments in which they grew. Knowledge about three dimensional crystalline lattices and the dynamics of their formation is fundamental to understanding and controlling larger scale crystal properties. Resulting applications are relevant in geology, biology, and material science.

#### *b) The Study of Crystalline Solids*

Studying crystalline solids is particularly important given their abundance in nature. Many geological mineral formations are crystals of inorganic ions such as calcium, sodium, phosphate, and sulfate. Managing the desirable or undesirable growth of such deposits is aided by an understanding of the dynamic processes affecting their atomic scale structure. Crystals also play significant roles within biology and medicine. The inorganic components of bone and teeth are primarily composed of hydroxyapatite, a crystal of calcium and phosphate

$[\text{Ca}_{10}(\text{PO}_4)_6(\text{OH})_2]$ .<sup>2</sup> Prevention and treatment of *ectopic osteogenesis*, the growth of bone-like crystals in adverse locations such as within cartilage and blood vessels, requires adequate knowledge about the remodeling processes of the hydroxyapatite lattice.<sup>2</sup> Microscopic crystalline properties can also be exploited for material science purposes. These include the design of new biomaterials, such as bioresorbable bone grafts, and novel nanotech devices. Again, controlling crystal structures for these applications requires understanding of both the atomic structure of crystalline solids, and the dynamic processes by which they form and degrade. Exploring these crystal properties is a challenging endeavor however, because visible light cannot resolve the nanometer and angstrom scale features of the lattice. The creative application of technology and indirect methods must be utilized to study crystalline materials.

Diffraction studies use x-rays, electrons, and neutrons to provide high resolution data about the three dimensional landscape of a crystal lattice. Due to the quantum effects prevalent at such small size scales, photons, electrons, and neutrons interact with the atoms in a crystalline lattice in a wavelike manner. Waves incident on different locations within the lattice bounce off the structure, constructively and destructively interfering when they are in phase and out of phase respectively. This produces a characteristic diffraction pattern with maxima and minima that depend upon the geometry of the lattice, the properties of its atomic constituents, and the incident angle of the x-ray, electron, or neutron beam. Upon bombarding a single crystal with a beam at all possible incident angles and measuring the resulting diffraction patterns, one can work backwards to define the lattice structure. This process is calculation intensive, but it provides a tremendous tool for determining the orientation of atomic and molecular subunits in a crystalline material. Also known as x-ray crystallography, this technique has allowed researchers to determine the structures of many inorganic crystals and to model the three

dimensional conformations of many biological macromolecules, which can also be crystallized under specialized conditions.

A diffraction image of the lattice provides part of the picture, but it is also necessary to determine how new material is incorporated into a crystal and how stable the structure remains under various conditions. Most inorganic crystals grow in aqueous environments saturated with their ionic constituents. Optical microscopy can be used to some extent here, by imaging bulk crystal growth or dissolution over long time periods. Simultaneously, precise chemical titration methods are utilized to determine how the chemistry of the solution changes. If the crystal has visible macroscopic cues, allowing its lattice orientation to be determined, these experiments can be used to approximate the rates at which constituents are bound to or dissociate from the crystal lattice. This empirical evidence can be compared with theoretical data to determine the dominating mechanism of crystal growth.<sup>3</sup> Unfortunately, this indirect method of observing growth and dissolution remains somewhat blind to the nanoscale phenomena occurring in reality. Only with the invention of scanning probe microscopy did researchers gain the means to directly observe the microscopic dynamics of crystalline materials.

Scanning probe microscopy is a generic category that describes a variety of related technologies aimed at imaging nanoscale topographies. The electron microscope is a common example, but it requires a conductive substrate, making it unsuitable for many materials unless they are coated in a metal such as gold. For non-conductive materials the scanning force microscope (SFM), also known as the atomic force microscope (AFM), is more applicable. SFM allows the user to physically interact with a surface in or out of solution, imaging the nanoscale landscape and imparting variable forces on the material at the same time. Since crystal growth and dissolution occurs at the exposed solid-liquid interface, scanning force microscopy provides

an ideal method to observe the related atomic events. In praise of this technology Mann et al. proclaimed:

“It is now possible to visualize the collective atomic motions and maneuvers, and elucidate the underlying mechanisms of crystal growth. Movies of crystal growth may not yet have reached the video shops but they remain fascinating to watch with or without a cold beer.”<sup>4</sup>

### *c) Scanning Force Microscopy*

Scanning force microscopy interacts with a surface via a small tip. The tip is adhered to a reflective gold cantilever and placed in contact with the substrate of interest. As the tip moves vertically up or down, the cantilever bends. The resulting movement causes a laser beam, incident on the back of the cantilever, to reflect at an angle related to the magnitude of vertical displacement. The beam is detected by a photodiode quadrant, which is capable of converting the vertical and lateral location of the laser spot into two voltage signals. These signals fluctuate as the tip is rastered about a selected area of the surface, experiencing vertical and horizontal deflections as it encounters bumps, pits, and other changes in topography. The data collected for each point on a selected area can be converted to a three dimensional image of the surface.

In order to create accurate spatial images, the SFM tip must move across a surface with high spatial resolution in three dimensions. This feat is accomplished using a piezoelectric scanner. Applied voltages across a piezoelectric material can induce changes in its length or shape. In the SFM, the tip/cantilever apparatus is connected to the base of a calibrated piezoelectric rod. Upon applying appropriate voltages across the rod, the tip can be moved with resolution on the order of nanometers in the horizontal  $x$  and  $y$  directions, and angstroms in the vertical  $z$  direction. Because of this high spatial resolution, it is more precise to map the surface

topography based on the voltage signal applied to the piezoelectric scanner instead of on the signal measured at the photodiode. As the SFM tip is moved laterally about a surface, deflections in the cantilever change the photodiode signal. A feedback loop causes rapid adjustment of the voltages supplied to the piezoelectric scanner, counteracting the tip deflection and returning the vertical photodiode signal to its baseline value. The three dimensional tip coordinate is calculated from the piezoelectric voltages and plotted in an SFM image.

Numerous scanning parameters can be adjusted to achieve different results using the SFM. Devices are primarily operated in one of two modes, tapping mode or contact mode. In tapping mode the tip is oscillated above the surface under control of the piezoelectric scanner. Capturing images using this technique minimizes the horizontal friction forces imparted on the sample as the tip scans across its surface. Contact mode requires that the tip touch the surface indefinitely. The tip will therefore impart some lateral friction on the surface as it sweeps about the scanned area. The magnitude of such stresses can be adjusted by changing the normal force imparted by the tip, which is accomplished by varying the baseline deflection signal at the photodiode and/or changing the cantilever's spring constant. In both imaging modes, scanning area and raster speeds can be adjusted. The resolution can be improved by decreasing the surface area scanned and the raster speed. Instead of scanning a two dimensional area, the tip can also be moved in a single lateral direction, either  $x$  or  $y$ , thereby traversing a cross-section of the surface. It is also possible to press the tip into the surface at a single  $x$ - $y$  coordinate. These are among the many options that can be manipulated to explore the intricacies of crystalline surfaces or other substrates.

Like most things, every crystal is different and some are more suited to scanning force microscopy studies. The most desirable feature for SFM is to have an extremely flat surface.

Especially in studies of crystals, where it is necessary to identify specific lattice directions and features of the exposed surface, rough samples are difficult to decipher. The best experimental substrates are cleavage planes found in certain crystal structures including mica, calcite, brushite, and gypsum. These planes are bonded together weakly due their particular orientation within the lattice structure, and can be freshly manufactured by wedging a razor blade into the edge of a sample just prior to imaging with SFM. The surfaces produced by cleaving these crystals offer ideal conditions for studying crystal dynamics.

#### *d) Crystal Growth and Dissolution Mechanisms*

The classical model of crystal growth describes a surface identical to those cleavage planes observed using SFM.<sup>4</sup> Flat regions of equivalent height are known as terraces. Steps separate two terraces layered on top of one another. Stable steps often correspond to directions within the lattice that are energetically favorable. If steps parallel to two different lattice directions intersect, they form a corner. In some cases an elevated terrace can be bound by steps on all sides forming an island, or a depressed terrace can be bound on all sides forming a pit. The most important features in growth and dissolution are called kinks and double kinks. These are essentially notches within an otherwise continuous step, where the atomic constituents of the lattice are missing. *Figure 2* is the projection of a theoretical crystal topography containing those features described above.

According to the classical model described by Mann, crystals grow and dissolve in a layer by layer process.<sup>4</sup> These phenomena occur in solution, where ions transition between solvated states and bound states in the solid lattice. Free energy arguments can be used to distinguish between growth and dissolution. Growth will occur when the free energy of the crystalline phase plus that of the final solution phase is lower than the initial free energy of

solution.<sup>5</sup> Equivalently, growth is associated with a negative free energy of solution, which is the difference between the energy required to break coordinating bonds in the crystal lattice and the energy associated with the hydrated ions and ion pairs formed in solution. Common thermodynamic derivations lead to equations [1] and [2], the solubility constant and free energy of solution at equilibrium, where growth and dissolution rates offset.<sup>4</sup>

$$K_{SP} = [M^+]_{eq}^n [X^-]_{eq}^m \quad [1]$$

$$\Delta G_S = -kT \ln K_{SP} \quad [2]$$

Here  $[M^+]_{eq}^n$  and  $[X^-]_{eq}^m$  correspond to activities, which can be approximated by the solution concentrations of the positive and negative ions respectively given an arbitrary crystal of chemical formula  $M_nX_m$ .  $k$  is the Boltzmann constant, and  $T$  is the absolute temperature. Under non-equilibrium conditions an activity product characterizes the solution composition.<sup>4</sup>

$$AP = [M^+]^n [X^-]^m \quad [3]$$

The magnitude of the free energy of solution, which determines whether growth or dissolution dominates, can be characterized by the supersaturation,  $\sigma$ , which is given by:<sup>5</sup>

$$\sigma = \ln(AP / K_{SP}) \quad [4]$$

When  $\sigma$  is greater than unity the solution is considered supersaturated and crystal growth is energetically favorable. For  $\sigma$  below one, the solution is undersaturated and conditions favor crystal diminishment via dissolution. This thermodynamic parameter provides an ideal method to predict whether growth or dissolution will occur. Predicting the rates of such phenomena is more complicated as they depend on the lattice geometry, the crystal's composition, the topography of the exposed liquid-solid interface, temperature, and solution chemistry.

Therefore, it is necessary to elucidate the atomic scale mechanisms controlling ion movement between the aqueous and solid phases.

Growth and dissolution are predicted to occur via equivalent, but reverse processes.<sup>6</sup> In supersaturated solutions the surface contains active sites of higher binding energy where ions have a high probability of incorporating into the lattice, as described by Mann.<sup>4</sup> Sites with the most potential bonding interactions for an incoming ion have the highest energies. Therefore, ions bind easiest to kinks, then corners, steps, and finally terraces. In order for a solvated ion to bind at one of these sites, it must first diffuse to and adsorb onto the crystal surface. Growth rates are often limited at this point, with some crystals' growth dependent on the rate of ion diffusion from the bulk solution to the surface, and others dependent on the reaction rate of ion adsorption.<sup>7</sup> Once associated with the crystal surface, ions can diffuse about terraces laterally until they coordinate with a step. Once attached to a step, the ion is limited to one dimensional diffusion along the step direction. As the ion reaches a kink site, it will finally bind to the lattice. When all local kink sites are consumed, new steps must be nucleated upon existing steps. Similarly, when an entire terrace has filled in and no step sites remain, new islands must be nucleated, an even more energetically unfavorable event. The rates of this layer by layer growth process can vary tremendously, even across different samples of the same material. Rates depend on the solution supersaturation and crystal size, and the number of kinks and defects exposed at the surface. Samples also tend to have many lattice planes exposed to the solution simultaneously, each of which experiences unique growth rates since each face has a different lattice geometry and associated energies. Scanning force microscopy allows direct observation of these localized atomic scale growth rates and mechanisms, which is fundamentally necessary in order to understand and control crystal growth and dissolution processes.

### *e) Applications of Scanning Force Microscopy*

The success of SFM in imaging atomic scale crystal dynamics is undisputed. Growth and dissolution processes have been observed extensively on surfaces of single crystal calcite ( $\text{CaCO}_3$ ) (reviewed by Astilleros et al) and gypsum ( $\text{CaSO}_4 \cdot 2\text{H}_2\text{O}$ ).<sup>3,6-9</sup> The results have verified the classical model of crystal growth and corrected some flawed conclusions from indirect chemical titration experiments. For instance, an analysis of larger scale crystal growth kinetics suggested gypsum grows via a spiral growth mechanism,<sup>10</sup> but SFM studies have only observed the layer by layer growth described above.<sup>3,7,9</sup> SFM observations have also provided qualitative evidence in support of the relative lattice direction stabilities on the (010) surface of gypsum, as predicted by the theoretical energy calculations of Weijnen et al.<sup>3,11</sup> Imaging crystal cleavage surfaces has yielded valuable insight regarding the nanoscale mechanisms of crystal growth on several substrates, but the SFM technology is not limited to passive observation of growth and dissolution.

In contact mode, force microscopy imparts vertical and lateral stresses on a crystal surface, allowing the user to actively manipulate ions in exterior lattice sites. The force of such interactions can be varied, along with the solution chemistry, to induce changes on an exposed crystal surface. This technique was utilized to study the (1014) face of calcite.<sup>12</sup> High contact forces promoted dissolution at step edges as the tip provided adequate energy to remove ions from the lattice. Similar phenomena were later produced on the (010) surface of brushite.<sup>13</sup> Rates of tip induced double kink formation, measured as a function of tip normal force, have yielded activation energies and activation volumes for double kink formation on calcite and brushite.<sup>12,13</sup> SFM has also been capable of tip induced growth. Precipitation was improved on tip contacted surfaces of gypsum and calcite when out of solution and in the presence of 10-35%

humidity.<sup>14</sup> *In situ* studies of calcite and brushite in supersaturated solutions showed that low contact force scanning can facilitate nucleation and crystal growth along step edges.<sup>15,16</sup> The proposed mechanism involves weakly adsorbed ions being swept by the tip across an elevated terrace and over a potential energy barrier at step sites.<sup>16</sup> Upon dropping onto a lower terrace the ions become coordinated at higher energy step and kink sites. Studies of brushite have concluded that the transition point between tip induced growth and dissolution phenomena occurs at a force of approximately 50 nN.<sup>16</sup> Manipulating crystal surfaces using SFM, either to promote dissolution or growth, increases our understanding of atomic scale mechanisms, and has potential technological applications including chemical mechanical planarization (CMP) processes.<sup>15</sup>

Tip induced growth and dissolution have been achieved on calcite and brushite as described above, but *in situ* SFM modulation of gypsum surfaces has not been extensively documented. While some mention has been given that tip induced dissolution<sup>13</sup> and growth<sup>17</sup> is possible on its surface, a thorough study has yet to be completed. Exploring these phenomena on the (010) face gypsum could provide valuable qualitative and quantitative information about natural atomic scale remodeling mechanisms on the gypsum surface. Furthermore, it could verify and improve those models that describe tip induced dissolution and growth processes. Controlled application of these techniques may be applicable on a variety of substrates, expanding the potential benefits. Those materials which prove better suited for planarization may yield atomically flat surfaces, while others may have suitable properties for the design of novel nanoscale topographies in nanolithography. Gypsum shares a closely related lattice structure with brushite and provides a suitable cleavage surface, making it an ideal substrate to continue exploring SFM manipulation processes on crystalline materials.

### *f) Properties of Gypsum*

Examining the surface of gypsum with SFM is particularly valuable because natural forms of the mineral are so abundant. It is the most prevalent natural sulfate, associated with limestone and shale deposits, and it is the main inorganic scale deposited in hydrocarbon reservoirs.<sup>3,9</sup> Used in building materials and wallboards, it is “arguably the most important of cement additives.”<sup>9</sup> Gypsum has also been used as a filler of bone defects and as a substrate for the synthesis of new hydroxyapatite in bone and tooth implants.<sup>18</sup> Greater comprehension about the dynamic processes involved in gypsum formation and dissolution could impact those techniques used to control mineral growth in the aforementioned fields.

The gypsum lattice assumes a monoclinic structure. The unit cell, as defined by the neutron diffraction studies of Pederson and Hemmingsen, has the lattice parameters  $a = 5.679 \text{ \AA}$ ,  $b = 15.202 \text{ \AA}$ ,  $c = 6.522 \text{ \AA}$ ,  $\beta = 118.43^\circ$ , and space group  $I2/a$ .<sup>19</sup> The lattice structure can be viewed online using the applet provided on the Mineral Web website.<sup>20</sup> The unit cell includes a double water layer at the planes equivalent to  $\frac{1}{2} b$  periodicity. Weak bonding between these water molecules results in the (010) cleavage plane.<sup>7</sup> Step heights on the (010) surface correspond to a single atomic layer, also equivalent to  $\frac{1}{2} b$  periodicity; therefore each terrace is separated by steps 7-8  $\text{\AA}$  in height, a distance verified by SFM imaging.<sup>6</sup> Gypsum solubility is 2.55 g/L at room temperature and in pure water, which corresponds to an equilibrium constant of  $K_{sp} = 2.28 \times 10^{-5}$ .<sup>21</sup>

According to previous SFM studies, dissolution and growth occurs on the (010) face of gypsum in a highly geometrical manner. Near equilibrium conditions, terraces and pits are almost exclusively bound by steps parallel to the [100] and [001] directions, which are equivalent to the crystallographic  $a$  and  $c$  directions respectively.<sup>7</sup> Step velocities, defined as

the rate of step movement perpendicular to the step direction during growth and dissolution, are not equivalent for the two directions. Steps parallel [100] move faster than those parallel to [001], so that surface topographies often take on an elongated geometry in the [001] direction parallel to the  $c$  axis.<sup>7</sup> This anisotropy in velocity between the fast/[100] step and the slow/[001] step can be explained in terms of the stabilities associated with different planes and directions within the gypsum lattice.<sup>9</sup> The (010) plane is most stable for the same reasons that it is a good cleavage plane. Plane (120) is the next most stable, so it grows relatively slowly, and on the (010) face it corresponds to the slow/[001] steps. Plane (011) is the third most stable, occurring in the fast/[100] zone on the (010) face. The (111) plane is next, corresponding to a rarely seen [101] step on the (010) face. Theoretical calculations predict the step energies for [100] = 0.353 eV/Å, [001] = 0.365 eV/Å, and [101] = 1.678 eV/Å.<sup>11</sup> Greater step energy corresponds to a greater likelihood of ion incorporation or loss, in growth and dissolution environments respectively, so these theoretical values qualitatively agree with the relative step velocities observed in SFM studies.

Several other noteworthy phenomena were observed in early force microscopy studies of gypsum. Step velocities were observed to change drastically depending on the topographical features in their immediate vicinity. When large concentrations of step edges were located nearby, dissolution velocities decreased.<sup>3,6,7</sup> These results support the findings of Christofferson and Christofferson who determined that gypsum growth is primarily dependant on the diffusion of ions within the bulk solution to the crystal surface.<sup>22</sup> In contrast, dynamics of the (1014) face of calcite are dependant on the surface reaction process by which ions bind to and dissociate from terraces.<sup>7</sup> Therefore, step velocities on calcite are independent of location and surrounding features. The gypsum surface also exhibited a temporary memory effect, where surface defects

affected equivalent  $x$ - $y$  locations on the topmost layers of the gypsum lattice. During dissolution, the formation of terrace vacancies and subsequent pits occurred at identical lateral positions.<sup>6,7</sup> It was concluded that the cleaving process contributed to linear defects, extending perpendicularly into the (010) face, which resulted in the redundant formation of etch pits on the surface.<sup>6</sup> The importance of local topography and memory effects must be kept in consideration while attempting to extract qualitative or quantitative data about dissolution and growth on gypsum.

## II. Hypothesis

We predicted that scanning at low normal forces, below 50 nN, and in supersaturated solution will promote material deposition and fill in existing etch pits on the (010) surface of gypsum. Normal forces above 50 nN were predicted to induce dissolution and rates should increase with decreasing supersaturation and increasing tip contact force.

## III. Methodology

Optically clear single crystal gypsum (selenite) was cleaved using a razor blade immediately prior to each experiment. In order to be mounted in the SFM apparatus,  $5 \times 5 \times 1$  mm<sup>3</sup> crystal plates were fixed to clean glass microscope slides using epoxy. To minimize growth and dissolution on exposed surfaces not corresponding to the (010) face, sample edges were sealed with the mounting epoxy, similar to the procedure described by Hall et al.<sup>9</sup>

Scanning force microscopy was performed in contact mode using a Molecular Imaging PicoScan AFM. *In situ* images were taken at room temperatures (22-25° C) using a Teflon reservoir clamped above crystal samples, which provided a liquid cell approximately 50  $\mu$ L in volume. Commercially available Si<sub>3</sub>N<sub>4</sub> cantilevers, with tip radii of ~40 nm, were used. Cantilevers all came from the same wafer and had spring constants of either 0.58 or 0.32 nN/nm. Tip normal forces were calculated by standard methods using these spring constants, the

photodiode baseline signal, and the SFM setpoint, a variable parameter. Image analysis was performed using the Molecular Imaging PicoScan software and ImageJ.

Almost all experiments were run in supersaturated  $\text{CaSO}_4$  solutions. Stocks of  $\text{Ca}(\text{NO}_3)_2$  and  $\text{MgSO}_4$  were prepared using reagent grade chemicals and distilled water, and micro filtered to remove impurities that could induce homogeneous solute precipitation. Combined in a 1:1 ratio and diluted with distilled water, these yield solutions supersaturated with respect to gypsum (see equations [3] and [4]). Mixing the imaging solutions was performed immediately prior to each experiment to prevent homogenous nucleation of  $\text{CaSO}_4$ .

In order to minimize local fluctuations of supersaturation during experiments, freshly mixed  $\text{CaSO}_{4(\text{aq})}$  was continually pumped through the SFM liquid cell. A Masterflex C/L micropump provided a flow rate of less than 1 mL/min. This low flow rate ensures laminar flow across the sample and minimizes any disruptions to the SFM probe. No adverse affects were observed in the SFM images due to the liquid flow.

## IV. Results & Discussion

### *a) Tip Induced Growth*

SFM induced growth was achieved on gypsum crystals in the presence of supersaturated solutions above  $\sigma = 0.56$ , with supersaturation  $\sigma$  described in equation [4]. Below this concentration little or no material deposition was observed on the (010) face, either by spontaneous mechanisms or tip induced ones. Similar to in previous experiments, spontaneous growth and nucleation were observed in solutions above  $\sigma = 0.93$ .<sup>6</sup> This spontaneous growth supplemented that induced by SFM scanning, leading to rapid topographical changes. These rapid events are difficult to capture since SFM is limited by slow image acquisition rates, as the rastering action must move the tip about the entire image area, which generally takes at least 60

seconds. Also, in contrast to the cleavage surface of calcite, gypsum growth is primarily rate dependent on the bulk volume diffusion of ions to the surface.<sup>22,23</sup> Previous SFM studies have confirmed that growth and dissolution rates of steps on the (010) face decrease in the local vicinity of other steps.<sup>6,7</sup> Because gypsum was highly sensitive to small changes in solution concentrations and local topography as described above, achieving a controlled environment conducive to tip induced growth proved a significant obstacle in achieving consistent results.

Despite the inherent challenges, our experiments provided convincing evidence that tip induced processes can improve the deposition of ions in etch pits on the gypsum surface. *Figure 3* shows the result of linear scanning across a monolayer pit, 7-8 Å in depth. This experiment was performed in supersaturated solution ( $\sigma = 0.56$ ) under no-flow conditions, where new CaSO<sub>4</sub> solution was not pumped through the SFM liquid cell. Immediately apparent is the presence of rounded features on the pits shown in image (a). Images taken of the surrounding topography confirmed the [001] direction of the slow step as diagramed on the image, but the fast step does not parallel the [100] direction as it normally does in solutions of lower CaSO<sub>4</sub> concentration. The rounded corners suggest that the stability of the [100] direction relative to other possible step geometries is insignificant, and a similar phenomena was previously observed by Hall et al.<sup>9</sup>

The complicated pit geometries were likely due in part to the high supersaturation during imaging and also because of the mechanisms that led to their formation. Since it is energetically unfavorable to remove ions from their highly bound states in a terrace, thereby nucleating a new pit, such features rarely formed spontaneously in supersaturated solutions. Bosbach et al. observed an abundance of pits on the topmost layers of several gypsum samples, and concluded that their formation was a result of linear defects caused by the cleavage process.<sup>6</sup> We rarely observed such phenomena. Instead, a drop of pure water was placed on the cleavage surface and

then immediately dried off using compressed air. These conditions encouraged the formation of a highly pockmarked surface, and would occasionally yield atomically flat terraces marred by a few isolated pits, one or two atomic layers in depth. This process produced the pits imaged in *Figure 3*, and likely contributed to their unique shapes.

After capturing image (a) in *Figure 3*, the SFM was operated in linear scanning mode, where the tip moved back and forth across the green line perpendicular to the fast steps of the smallest pit. The tip was maintained in contact with the surface at a normal force of 12 nN. In linear scanning mode the  $y$ -dimension of tip movement was fixed and images show a cross-sectional plot of the  $x$  and  $z$  tip location versus time. This made it possible to observe the fast steps of the small pit pinching together as scanning proceeded. After approximately 3000 back and forth traverses of the tip, the small pit was completely filled and a three dimensional image (b) was captured. Surprisingly, the other pits in the image actually increased in area, if only slightly.

The SFM promoted growth of the lattice could be explained by the mechanisms previously described for tip induced growth on brushite and calcite.<sup>15,16</sup> According to these studies the tip interacts with ions adsorbed onto upper terraces, and sweeps them over a potential barrier into pits. Ions can then attach to steps, diffuse to kink sites, and bind to the lattice. However, during linear scanning, as was done in our experiments, the tip only traverses a small surface area, minimizing the opportunities for it to interact with adsorbed species. Lateral sample drift in the  $y$ -direction during the linear scan could have slightly increased the probability of such interactions leading to an increased growth rate. Furthermore, the incorporation of adsorbed ions into the lower pit would improve the probability of solvated ions adsorbing onto regions along the scan line. The diffusion of species towards these sites could have depleted

local concentrations in areas removed from the linear scan. This could account for the slight dissolution observed at the boundaries of the larger pits, especially given that the gypsum surface is highly sensitive to small changes in solution chemistry due to local topographical features.

Another unique pit formed by the water droplet method is shown in image (a) of *Figure 4*. Again, this pit is partially bound by identifiable [001] steps, but does not have distinguishable features parallel to the [100] direction. In this experiment scanning was performed about the entire area surrounding the pit as shown by the sequence of images (a) through (e), with the fast raster direction perpendicular to the slow step. The solution was supersaturated ( $\sigma = 0.56$ ) and the contact force was maintained at 10 nN. This pit filled in rapidly as material appeared to accumulate along the [001] steps. In image (e) it is apparent that the pit filled in completely, leaving no visible defects on the (010) surface. Locations far removed from this pit did show signs of spontaneous growth, but at lower rates.

The pit shown in *Figure 5* was formed in a much more controlled manner than those described above. The gypsum sample was first placed in slightly undersaturated solution ( $\sigma = -0.013$ ) for five minutes to promote the expansion of any existing pits or those formed as a result of cleavage defects. Subsequently, the solution was replaced with supersaturated solution ( $\sigma = 0.56$ ) to encourage crystal growth. The single layer pit in image (a) had plenty of time to stabilize and its steps almost perfectly match the geometry of a pit bound by the [001] and [100] lattice directions. After centering the SFM scan area on the pit, the sequence of images (a) through (f) were taken with a tip normal force of 5 nN and the fast raster direction was perpendicular to the [001] step. Scanning did not completely fill in the pit, but signs of tip induced growth at the acute corners were unmistakable.

The phenomenon observed in the sequence of images shown in *Figure 5* was observed on several gypsum samples. By comparing the change in the pit size before and after scanning with the spontaneous growth at other pits and steps, it was obvious that SFM improves the deposition of material on the (010) face of gypsum. In most cases, scanning perpendicular to the slow step promoted material accumulation primarily in the acute pit corners. Growth appeared to proceed parallel to the [001] direction, from acute corner to obtuse corner, and the pits pinched together as the distance between opposing slow steps diminished. These qualitative results might signify an energetic discrepancy between the binding sites at the acute and obtuse corners of gypsum pits. Improved bonding interactions with neighboring ions in the lattice or steric hindrances minimizing the accessibility of water molecules to bound ions could explain why new steps prefer to nucleate at the acute corner. These hypotheses might be confirmed by energetic modeling of the crystal lattice, but the required calculations have not been performed here.

Unfortunately these experiments do not provide quantitative evidence in support of the tip induced growth mechanisms described in previous studies of brushite and calcite.<sup>15,16</sup> Obviously the tip does aid in relocating ions to the steps bounding etch pits, so making SFM induced growth possible on gypsum. Unlike the hypothesized figure of 50 nN, it appeared that induced growth required tip contact forces below 20 nN for supersaturations between  $\sigma = 0.56$  and  $\sigma = 0.93$ . It was not determined whether material accumulated on upper terraces adjacent to the pit steps, which would support the existing hypothesis that ions must traverse an Ehrlich-Schwoebel type energy barrier in diffusing down steps.<sup>15,16</sup> The challenge of obtaining consistent pits and growth conditions also prevented systematic studies about how growth rates depend on the ratio of surface area scanned within versus outside of a pit. Tip induced pit formation on the (010) gypsum surface, which will be described below, may prove conducive to

such studies. Future work should seek to quantify the effects of factors including scan size, scan orientation, and normal force on growth rates to improve our understanding of SFM induced material deposition. The accomplishments described above have confirmed that tip induced growth is possible, and that such techniques are capable of manufacturing defect free atomically flat regions on the (010) face of gypsum.

*b) Tip Induced Dissolution*

Dissolution rates on the surface of gypsum varied greatly with solution chemistry. Step dissolution was observed on the (010) face for supersaturations up to  $\sigma = 0.56$ . This may seem surprising given that supersaturated solutions favor crystal growth. However, thermodynamic predictions apply to the overall tendencies for macroscopic growth, and localized microscopic inhomogeneities may favor dissolution.<sup>3</sup> Furthermore, the dissolution of gypsum steps above equilibrium concentrations may reflect the tendency of ions on the crystal surface to rearrange into the most energetically stable geometries upon exposure to solution, similar to the phenomena previously observed by Hall et al.<sup>9</sup> The rate dependence of gypsum dissolution on volume diffusion, as described previously, also makes observed dissolution highly sensitive to the density of steps on the local topography. These factors likely contributed to the variation of spontaneous dissolution rates observed on different gypsum samples in identical chemical environments.

Tip induced wear drastically increased dissolution rates on the (010) face, so it was advantageous to perform experiments in supersaturated solutions, where ions were less readily removed from the lattice. The reduced dissolution rates under these conditions made it more feasible to observe the SFM induced phenomena given the slow imaging rates of scanning force microscopy. In solutions at or above  $\sigma = 0.56$  tip induced dissolution was less effective. The

two methods of tip induced dissolution successfully employed were the formation of wear tracks and indentation pits.

Wear tracks were produced by performing linear scanning in a direction perpendicular to existing steps. *Figure 6* depicts the most commonly observed results in supersaturated solution ( $\sigma = 0.46$ ). The primary feature in image (a) is the corner outlined in white, which is formed by the intersection of a slow step parallel to the [001] direction and a fast step. The difference in height between the higher and lower terraces at the corner corresponds to a single step, one atomic layer in depth. The dashed double arrow head approximately perpendicular to the [001] step represents the path of the tip during linear scanning. Images (d) and (e) show the cross-sectional plots of tip deflection observed during the linear scanning, with scan number and time increasing from the top to bottom of each image. In (d) the tip contact force was maintained at approximately 20 nN, the regular force used during imaging. Notice that [001] step, identifiable by the light line in the center of the image, does not move during the 15 back and forth passes of the tip under these conditions. In image (e) the tip normal force was increased to 150 nN for approximately 25 sweeps of the tip. Image quality decreases with increasing scanning force, so the location of the [001] step has been identified by the white dotted line. The higher tip force immediately caused retreat of the step towards the right of image (e). This produced a linear wear track into the [001] step, approximately equivalent to the location of the dashed arrow in image (a).

Scanning for image (b) was initiated approximately 38 seconds after the termination of linear scanning in image (e). This delay was unavoidable, as the SFM settings, including scan area and tip normal force, required adjustment and the center of the image had to be relocated in order to reflect those conditions seen in image (a). Unfortunately this down time limits the

ability to observe the immediate effects of tip induced wear track formation. Comparing images (a), prior to linear scanning, and (b), following wear track formation, it is apparent that dissolution was increased at locations along the [001] step removed from the site of tip interaction. These apparent “bursts” of dissolution at sites extending beyond the edges of the original wear track were also observed on brushite and calcite.<sup>12,13</sup> In image (c) the dissolution has ceased as the steps have completely remodeled, forming a corner synonymous to the one observed in image (a). Notice that the other steps in the sequence of images, which were not manipulated by high force tip scans, show no signs of spontaneous growth or dissolution. The massive dissolution, observed between images (a) and (c), must therefore be attributed to the wear track formed by the SFM tip.

The images in *Figure 7* outline a similar example of tip induced dissolution in supersaturated conditions ( $\sigma = 0.46$ ). The pit shown in image (a) originated as an elongated parallelogram bound by the [001] and [100] steps shown. The enlarged upper left corner was the result of tip induced wear track formation and subsequent dissolution. The steps have re-equilibrated by the time of capture of image (a), and the [001] and [100] directions are clearly visible despite the slightly complex pit shape. High force line scans (~275 nN) were performed along the length of the dashed double arrow shown in the image. Once the location of the [001] step was observed to retreat from the cross-sectional images obtained during linear scanning, thereby confirming wear track formation, the capture of image (b) was initiated, approximately 24 seconds after the start of linear scanning. Dissolution was once again improved at locations distant from the wear track. Image (b) indicates that the local step geometry was significantly destabilized by wear track formation, resulting in the jagged features present in the lower right of the pit. These features disappear by the time image (c) was captured, at which point the pit is

once again bound by stable steps parallel to the [001] and [100] directions. Little dissolution occurs along those steps that were not damaged by tip wear, confirming that the dissolution phenomenon observed is SFM induced.

The dissolution processes observed in *Figures 6* and *7* can be explained by the energetically unstable features formed by the presence of a wear track. The SFM tip can form a wear track by removing individual ions or several ions at a time from steps. Therefore, the tip induces double kink formation as it removes ions from their bound states within continuous steps. As the tip etches further into an elevated terrace, more and more kinks are formed. The edges of the linear wear track become lined by these highly energetic lattice sites, which are prone to dissolution. The removal of ions from kink sites along the wear track exposes neighboring ions as new kink occupants. In some cases the removal of ions from adjacent locations can cause kinks to line up forming small steps or corners, which are slightly more stable and temporarily stationary. Inevitably, kinks will move towards the corners of a pit until they terminate as part of an existing step. Material adjacent to the wear track will dissolve in this manner until a stable pit geometry is achieved. A similar mechanism was proposed by Park et al.<sup>12</sup> In *Figure 7* image (b) the dissolution process was captured showing jagged features of the extended wear track correspond to thousands of microscopic kinks and corners. Image (c) displays the final stable geometry achieved when all kinks became incorporated into stable steps.

Surprisingly, the extended dissolution away from wear tracks on the (010) surface of gypsum appeared to occur much faster than in previous studies on brushite and calcite. In both *Figure 6* and *7* the dissolution proceeded so quickly that the steps had re-equilibrated within 205 and 320 seconds of wear track formation, respectively. Scudiero et al. observed rapid dissolution

bursts of up to  $1 \mu\text{m}^2$  between sequential images on brushite.<sup>13</sup> In *Figure 6*, over  $10 \mu\text{m}^2$  of material dissolves between images (a), before the wear track formation, and (b).

Another interesting phenomenon observed was the tendency for dissolution to proceed away from the wear track with greater magnitude in one direction than the other. In *Figures 6* and *7* it is apparent that a greater volume of material dissolved on one side of the wear track compared to the other. This might be explained by a discrepancy in the kink geometries on the two sides of the tip wear track. Perhaps the orientation of linear scanning with respect to the lattice geometry causes the ions on one side of the wear track to assume kink sites more likely to pile up on one another forming a stable step. This could explain why the lower edge of the wear track dissolved less than the upper one in *Figure 6*. Each assumed an equivalent final geometry, but the lower one did so adjacent to the wear track site while the upper one was a result of kinks terminating along a previously existing step.

Future studies should examine the process of extended dissolution, beyond the tip induced wear track, in more depth. Improving image acquisition rates during experiments or finding better suited conditions for slowing the dissolution process on the gypsum face would be desirable. Imaging the dissolution of wear tracks across the steps bounding small pits in solutions of greater supersaturation might provide opportunities to identify the intricacies of the dissolution processes, providing verification of the mechanisms proposed above. After observing the astonishing dissolution rates following wear track formation on calcite, Park et al claimed that “further study of this phenomenon is thus warranted.” A similar conclusion must be drawn from the gypsum results presented above.

### c) Modeling Tip Induced Wear Track Formation

It is productive to assay the possible mechanisms by which the tip removes material during the initial wear track formation. This was achieved for surfaces of brushite and calcite by determining the force dependence of the tip induced etching process.<sup>12,13</sup> Those studies modeled wear track growth rate,  $V$ , versus tip contact force using the Zhurkov–Arrhenius expression shown below:

$$V = V_0 \exp\left(-\frac{E_{act} - v^* \sigma}{kT}\right) = V_0' \exp\left(\frac{v^* \sigma}{kT}\right) \quad [5]$$

Parameters  $E_{act}$  and  $v^*$  correspond to the activation energy and activation volume required to nucleate a double kink (respectively),  $k$  is the Boltzmann constant,  $T$  is the absolute temperature in Kelvin, and coefficients  $V_0$  and  $V_0'$  are constants. The maximum tensile stress  $\sigma$  at the edge of a spherical indenter of radius  $r$  is given by the Hertz relation

$$\sigma = \frac{(1 - 2\nu)}{\pi} \left( \frac{2F_N E^2}{9(1 - \nu^2)^2 r^2} \right)^{1/3} \quad [6]$$

where  $F_N$  is the force applied to the indenter. Use of this relation to represent the stress assumes a spherical tip and elastic behavior for the tip-surface interactions. Scudiero et al. and Park et al. both note that according to Saint Venant's principle, stress induced dissolution will occur within a few radii of the tip location, so the average stress experienced at the surface will be lower than that predicted by equation [6]. Parameters  $\nu$  and  $E$  correspond to Poisson's ratio and Young's modulus, respectively. Upon fitting equation [5] to relevant data, it was determined that the double kink activation volumes on calcite were  $39 \text{ \AA}^3$  at slow steps and  $60 \text{ \AA}^3$  at fast steps.<sup>12</sup> Furthermore, the measured value of  $V_0'$  was used to approximate the double kink activation

energy as 0.8 eV. On brushite, double kink activation volumes were calculated to be  $62 \text{ \AA}^3$  for the [101] steps,  $48 \text{ \AA}^3$  for the [201] steps, and  $41 \text{ \AA}^3$  for the [001] steps.<sup>13</sup>

We attempted to achieve similar results on the (010) surface of gypsum by systematically assaying the influence of contact forces on etching rates during wear track formation.

Experiments were performed across both the slow step parallel to the [001] crystallographic direction, and across fast step, which normally parallels the [100] direction. Since the fast steps are more readily dissolved by the tip, we elected to study the two steps in different supersaturations. The slow steps were etched in solutions of  $\sigma = 0.24$ , while the fast steps were etched in solutions of  $\sigma = 0.46$ . These conditions provided optimal dissolution rates for observation with the SFM; however, since the two steps were assayed in different environments quantitative comparisons of the observed results are difficult to interpret. All experiments involved wear track formation across isolated monolayer steps in order to minimize any influence that local topographical features might have on tip induced dissolution rates. Linear scanning was always performed perpendicular to the step direction.

*Figure 8* outlines the results of an etching experiment performed across the [001] step in slightly undersaturated solution ( $\sigma = -0.013$ ). Images (a) through (f) show the cross-sectional images resulting from linear scanning across the step, and time increases from the bottom to top of each image. The step location is clearly visible as the boundary between the darker and lighter regions. Each image was captured using a different contact force between 4 and 73 nN. Etching rates were determined by measuring the change in the  $x$ -coordinate of the step between the beginning and end of the linear scanning. In *Figure 8* the etch rates successively increases between images (a) and (f) as the normal force was gradually incremented. This procedure was applied on other gypsum samples to yield the data shown in *Figures 9* and *10*.

Results from wear track experiments across the [001] step in supersaturated solution ( $\sigma = 0.24$ ) are shown in *Figure 9*. The etching rate is plotted versus contact force for seven individual experiments performed on unique crystal samples. Bold squares (■) denote the average growth rates at common normal forces. Variation between each data set increases at larger contact forces, as evident by the error bars that represent a single standard deviation from the mean. Despite this, each individual experiment produced a relatively uniform data trend that was adequately modeled by equation [5]. In fact, only one data set had a coefficient of correlation below 0.99 with  $R^2 = 0.95$ . The dashed line in *Figure 9* represents a least squares fit of equation [5] to the averaged data, with  $R^2 = 0.997$  suggesting that it accurately defines the observed results.

*Figure 10* shows an equivalent plot for etching experiments on the [100] step and in solution of  $\sigma = 0.46$ . The three data sets all follow similar exponential trends, and the average data is accurately modeled by equation [5] ( $R^2 = 0.995$ ), as diagramed with the dashed line. Once again, variation between different experiments increased with contact force.

Fitting equation [5] to data shown in *Figures 9* and *10* permitted calculations of the double kink activation volumes on gypsum, as in the case of brushite and calcite.<sup>12,13</sup> Calculations were performed using values of the Poisson's ratio ( $\nu = 0.27$ ) and Young's modulus ( $E = 25$  GPa) averaged from several gypsum samples, as obtained by Karacan and Yilmaz.<sup>24</sup> The calculated activation volumes were smaller than those observed on the other materials by two orders of magnitude. For the slow step the average activation volume was  $\nu^* \approx 0.11 \pm 0.019 \text{ \AA}^3$ , and for the fast step  $\nu^* \approx 0.11 \pm 0.001 \text{ \AA}^3$ . Since these volumes are essentially equal, it suggests that the tip interacts with equivalent ionic species during the etching process on both the fast and slow steps. Unlike the data obtained on brushite and calcite, the activation volumes

observed on gypsum are much smaller than the calcium and sulfate ions within the crystal lattice, so it is not clear which ion, if any, is primarily affected during wear track formation.

Modeling the data with equation [5] also allows approximation of the activation energy associated with double kink formation. Following the calculations made by Park et al, we will approximate that the coefficient  $V_0$  corresponds to the product of a typical vibration frequency within the lattice ( $10^{13} \text{ s}^{-1}$ ) and the linear displacement equivalent to the removal of a single lattice constituent from a step.<sup>12</sup> Given the lattice spacing in gypsum, the displacements following removal of a single sulfate anion from the [001] and [100] steps are 3.3 Å and 2.8 Å respectively. Provided values for the prefactor  $V_0'$ , which are calculated from the trendlines shown in *Figures 9* and *10*, it is possible to estimate the activation energy using the following relation:

$$E_{act} = -kT \ln(V_0' / V_0) \quad [7]$$

Our results indicate double kink activation energies of  $0.8 \pm 0.08 \text{ eV}$  and  $0.9 \pm 0.02 \text{ eV}$  for the [001] and [100] steps respectively. The activation energies for double kink formation on gypsum are similar to the activation energy of 0.8 eV calculated for steps on the (1014) surface of calcite.<sup>12</sup>

Upon comparing the two gypsum steps, it seems surprising that the fast step is associated with higher double kink activation energy. Higher activation energies typically correspond to slower dissolution. The discrepancy is probably due to the different solutions employed in the two measurements. Supersaturation impacted the rate of wear track formation on both steps and at all contact forces. Since dissolution was slower at higher supersaturations, and since the same value of  $V_0'$  was assumed for the fast and slow steps in equation [7], the estimates of double kink

activation energy will depend on solution concentration. If wear track experiments were performed across [100] in identical environments as the [001] experiments shown in *Figure 9* were, with  $\sigma = 0.24$ , the estimated fast step activation energy would likely be lower than 0.8 eV. Equivalently, if [001] experiments were performed in  $\sigma = 0.46$  solution, the activation energy estimate for the slow step would rise above 0.9 eV. Future experiments should measure tip induced wear as a function of solution concentration, at supersaturations where dissolution rates are neither too fast nor too slow for SFM analysis of the two steps. This would permit direct comparison of the double kink activation energies and the prefactors  $V_0$  corresponding to the two steps.

#### *d) Pit Formation by Tip Indentation*

The vertical stress applied by the SFM tip was also observed to induce material solvation by an indentation-like process. In contrast to wear track formation, which removed material from existing steps, the indentation phenomena involved the nucleation of pits within previously continuous terraces. This process often required extreme conditions with respect to the mechanical and chemical environments. Pit formation was only observed for tip normal forces greater than 200 nN. Pits were rarely formed in supersaturated solutions, and were more readily manufactured in solutions near equilibrium ( $\sigma = 0$ ).

*Figure 11* shows the result of a tip indentation experiment in supersaturated conditions. Image (a) shows the atomically flat surface topography prior to indentation. During indentation the SFM tip was fixed at the  $x$ - $y$  location of the white arrow and pressed into the surface with a normal force of 270 nN. After 10 seconds the contact force was reduced for imaging. The pits in image (b) were observed immediately following the initial indentation. Steps parallel to the [001] direction are clearly visible, but the fast steps remained jagged and undefined even upon

capture of image (c). Each pit is a single atomic layer in depth. The gypsum surface was scoured for other signs of damage within several microns of the tip indentation location, but the terrace remained in tact except for the pits shown in image (b). This suggests that stresses in the immediate vicinity of the tip caused the removal of ions from the exposed (010) surface.

Tip induced pit formation was even easier to achieve in solutions of lower concentrations. *Figure 12* shows two pits formed by tip indentation in undersaturated solution ( $-\sigma = 0.013$ ). The pit formed in image (a) was the result of a 200 nN contact force, and the one in image (b) was the result of a 210 nN contact force. Both pits are elongated in the crystallographic  $c$  direction parallel to their slow steps, a common feature of gypsum pits observed under dissolution enhancing conditions. Cross-sections of the two pits were taken along the green lines and are shown below their respective images. The pit in image (a) is approximately 8 Å in depth, corresponding to a single atomic layer, while the pit in (b) is likely two or three layers deep. In both cases the local topography surrounding the manufactured pits remained unaffected by the indentation process.

Tip induced pit formation may form via mechanisms similar to tip induced wear track formation. Removing ions bound within a terrace is significantly more difficult than nucleating double kinks at steps, but the higher tip contact forces must provide adequate energy to remove ions within several radii of the tip. From equation [6], a 200 nN normal force corresponds to a maximal tensile stress of 0.4 GPa at the edges of the SFM tip. If this successfully removes enough ions from the surface a pit can be nucleated. Ions at the edges of such pits will likely occupy exposed lattice sites, making them prone to immediate dissolution. Only when the pit has achieved a stable geometry, like the rhombus bound by the [001] and [100] steps, will dissolution cease. This could explain why the pits shown in *Figures 12* and *13* are much larger

than the area contacted by the pit. We have already described how dissolution proceeds rapidly away from unstable edges of wear tracks, so it is not surprising that a significant amount of material was removed between images (a) and (b) of *Figure 11* following the nucleation of a non-uniform pit.

The tip indentation process described above may prove extremely useful in future studies of the gypsum surface. It would be worthwhile to explore the pit formation process in greater depth. This could include further exploration of how pit formation depends on contact force and supersaturation. Alternatively, the mechanisms of tip indentation could be taken for granted, and the process used to form pits for other studies of tip induced growth and dissolution. Indeed, one of the greatest obstacles we faced was the consistent production of isolated pits on the (010) gypsum face and this tip indentation process seems an obvious solution.

## **V. Conclusions**

Explorations of SFM induced phenomena on the (010) face of gypsum proved successful. Similar to previous experiments performed on brushite and calcite, we observed tip induced growth and dissolution. At contact forces below 20 nN and in supersaturated solution, the SFM tip increased material deposition within monolayer etch pits. This process facilitates the filling of atomic scale gauges on the gypsum surface. Contact forces above 20 nN were conducive to removing ions bound to the crystal lattice. Linear scanning across steps caused the formation of wear tracks, and subsequent massive dissolution bursts extending to areas far removed from the locations contacted by the tip. Wear track growth was observed to increase with elevated tip normal forces, and the results were accurately modeled by a Zhurkov–Arrhenius expression previously applied in studies of brushite and calcite. This model permitted calculation of the activation energy and activation volume associated with tip induced double kink formation on

steps of the gypsum surface. Tip induced dissolution was also observed via a previously undocumented indentation process. Pressing the SFM tip into atomically flat terraces at normal forces above 200 nN caused the nucleation of stable pits on the (010) gypsum face. All of these processes can be exploited in further exploration of the gypsum surface and SFM controlled phenomena. Additionally, they provide methods for the manufacture of atomically flat surfaces and other novel nanoscale topographies using mechanical and chemical stimulation. Biomedical applications seeking to control biomineralization processes within joints, bones, and implanted tissues may also be relevant.

## **VI. Acknowledgements**

This work was supported by a Washington State University College of Sciences Undergraduate Research Minigrant. I thank my advisor Dr. Tom Dickinson for his knowledge and support. I also thank Steve Langford, Forrest Stevens, and Ann McEvoy for their guidance and contributions to the project.

## VII. Appendix: Figures

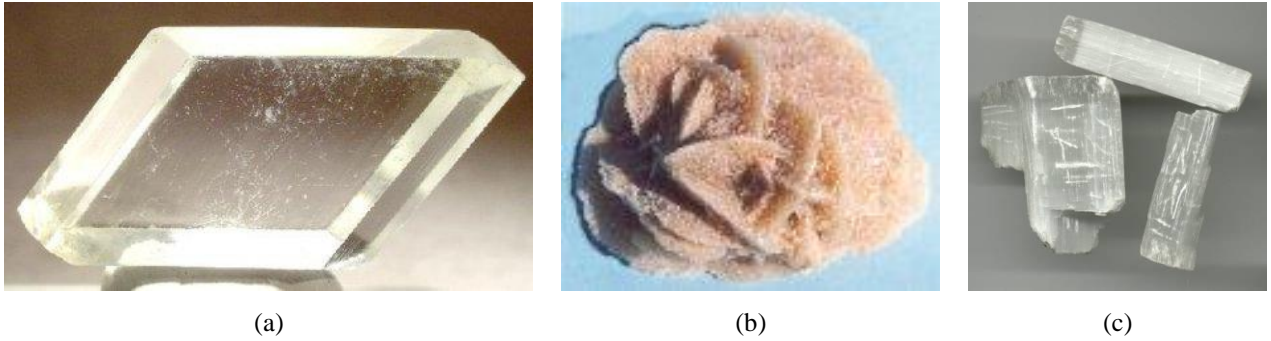


Figure 1. Natural forms of gypsum include (a) selenite,<sup>25</sup> (b) desert rose,<sup>26</sup> and (c) satin spar, also known as alabaster.<sup>27</sup>

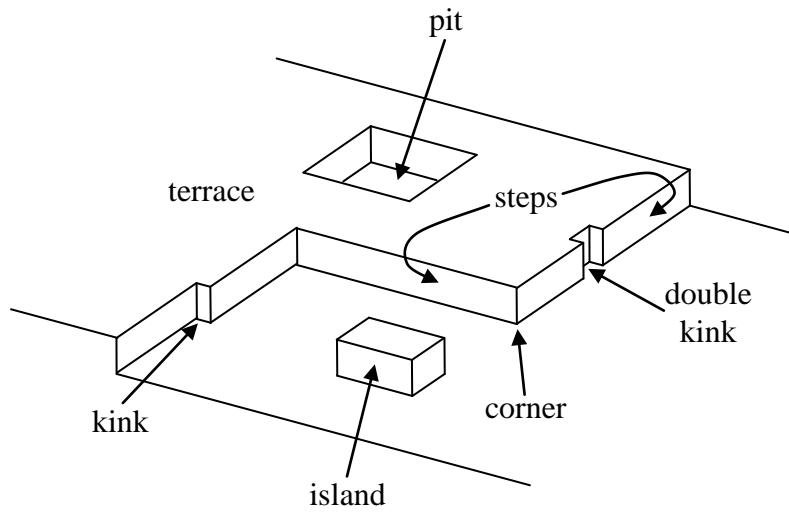
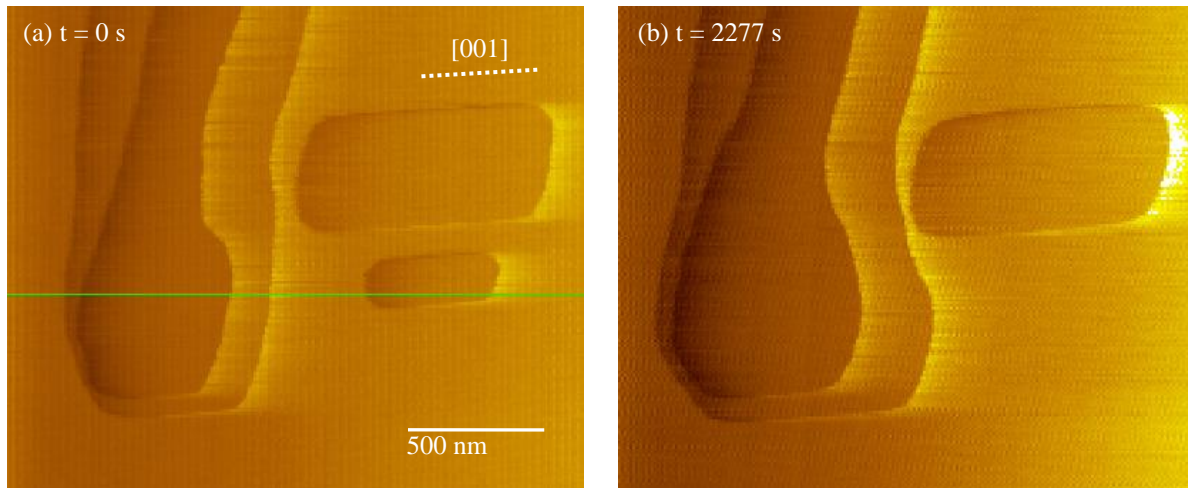
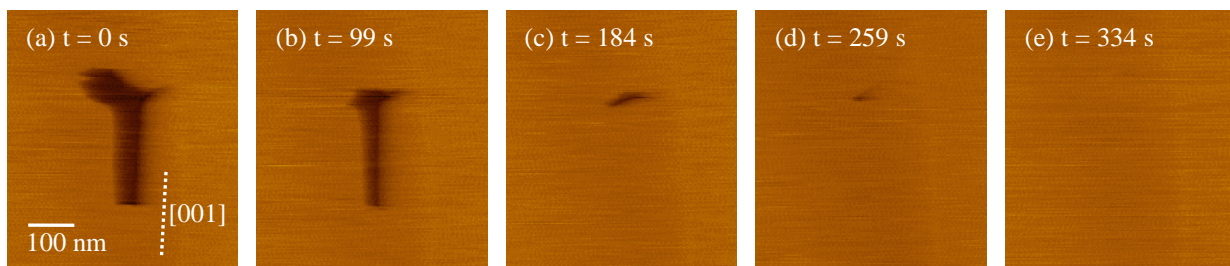


Figure 2. Projection of an ideal crystal topography.



*Figure 3.* These three pits were imaged in supersaturated  $\text{CaSO}_4$  ( $\sigma = 0.56$ ). Immediately following the capture of image (a), linear scanning was performed along the green line using a contact force of 12 nN. Scanning occurred approximately parallel to the [001] direction shown in image (a) such that the tip passed across the fast steps of the smallest pit, which are not exactly parallel to the crystallographic [100] direction in this case. After 2277 seconds of scanning, equivalent to approximately 3000 sweeps of the tip, the small pit had completely filled in as shown in image (b).



*Figure 4.* This abnormally shaped pit is only partially bound by [001] steps. Scanning about the area around the pit was performed in supersaturated solution ( $\sigma = 0.56$ ) with a normal force of 10 nN. After five successive scans shown in images (a) through (e) the pit was completely filled in

leaving no visible signs of surface defects.

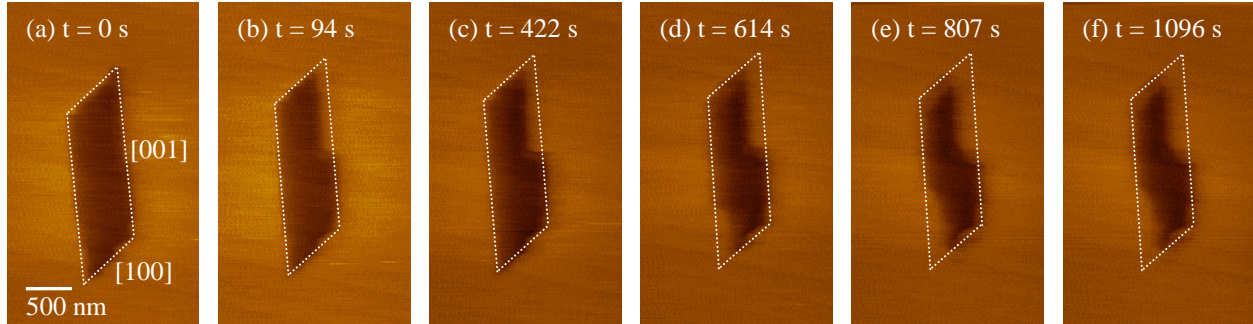


*Figure 5.* The monolayer pit was initially bound by steps parallel to the [001] and [100] lattice directions shown by the dotted outline in images (a) through (f). Scanning in supersaturated  $\text{CaSO}_4$  solution ( $\sigma = 0.56$ ) and with a normal force of 5 nN caused the pit to diminish in area as material accumulated primarily in the acute corners. The pit had not completely filled in after the sixth image (f), but crystal growth is visible and it exceeded growth rates observed on regions surrounding the scanned area.

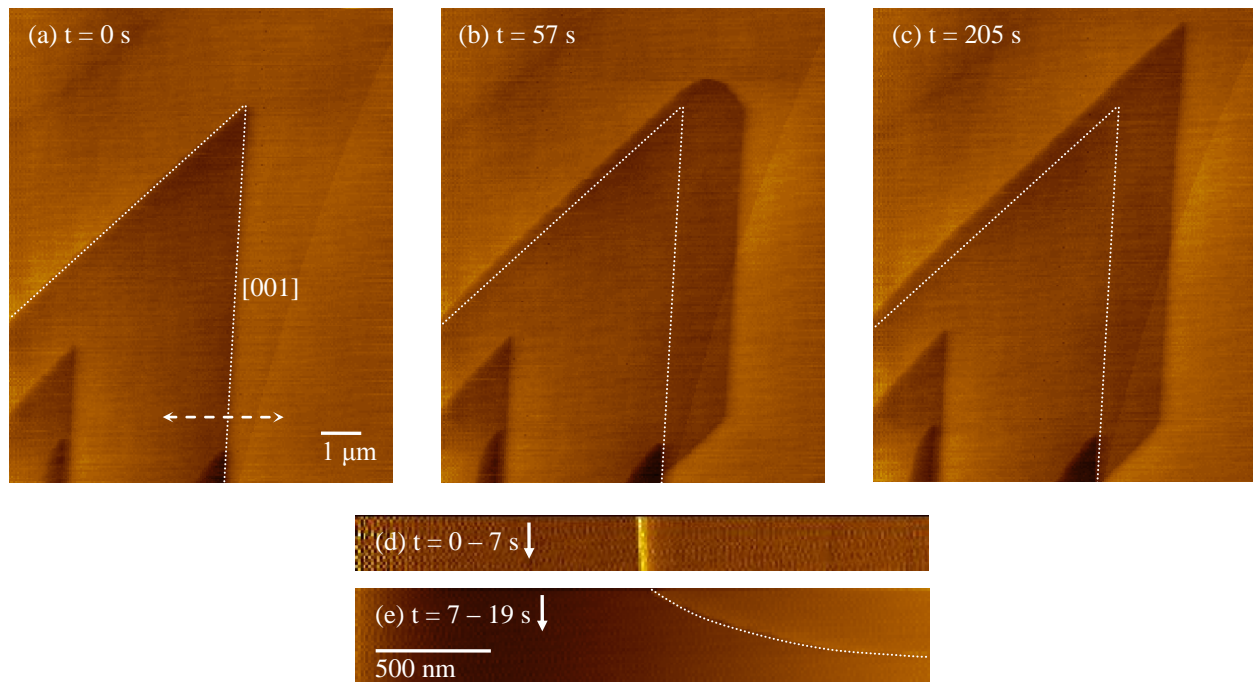


*Figure 6.* This series of images shows the effect of high force linear scanning across the slow [001] step in supersaturated solution ( $\sigma = 0.46$ ). Image (a) shows the initial pit bound by the

[001] step and a fast step. The acute angle formed at the intersection of these two steps is smaller than the  $62^\circ$  characteristic of a [100]/[001] corner, so the fast step observed is not equivalent to the [100] step. The dashed arrow in (a) represents the location of high force linear scanning, which occurred immediately prior to capturing image (b). Images (d) and (e) show the cross sectional images obtained during the linear scanning process, with time increasing in the downward direction. Imaging conditions were maintained with a normal force below 20 nN in (d), and the step location remained static. In (e) the force was increased to 150 nN for approximately 25 back and forth scans of the tip, immediately causing the step profile to wear away towards the right of the image. Image flatness and contrast are adversely affected when scanning at high normal forces, so the dotted white line has been added at the location of the [001] step edge to aid in visualization. Images (b) and (c) show the topography following the linear etching process. Dissolution proceeded rapidly away from the location of the tip wear track until a stable geometry, similar to that of the original pit, was observed in image (c).

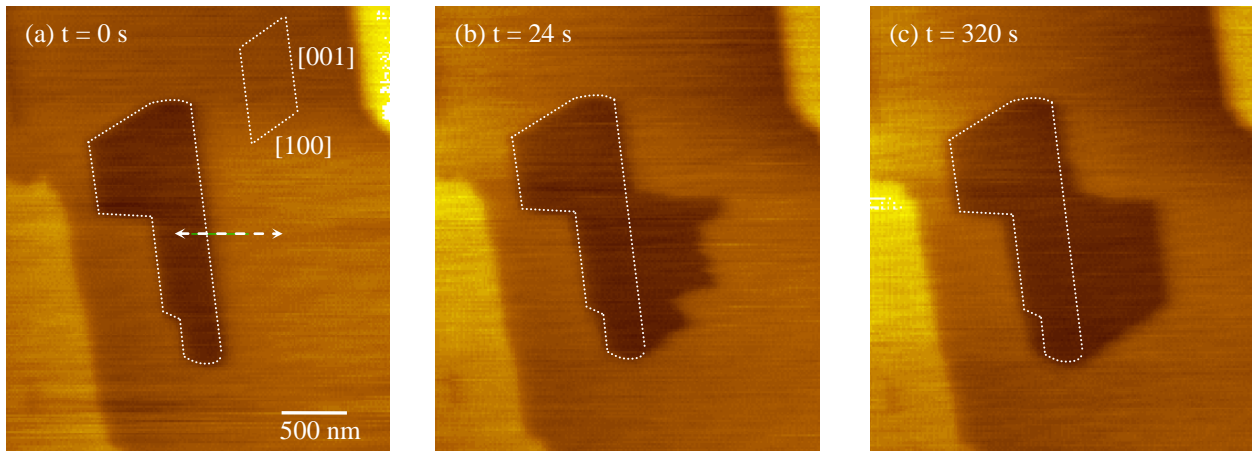


*Figure 7.* High force linear scanning at approximately 275 nN was performed across the [001] step in supersaturated solution ( $\sigma = 0.46$ ) beginning after the capture of image (a). The dashed arrow in (a) shows the location of linear scanning. Image (b) shows dissolution proceeding away from the original wear track location. Corners appear to have dissolved along the [100]

direction, until they terminated forming a new [001] step as seen in image (c). Little spontaneous dissolution occurred at locations distant to the tip induced etching event.

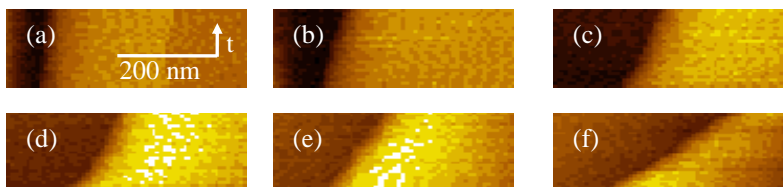


*Figure 8.* Images (a)-(f) show cross-sectional plots of step location versus time, resulting from linear scanning perpendicular to the [001] step in  $\text{CaSO}_4$  solution ( $\sigma = -0.013$ ). In each image time increases for approximately 9 seconds from the bottom to the top. Tip normal forces were varied in each image as follows: (a) 4, (b) 21, (c) 31, (d) 42, (e) 52, and (f) 73 nN. Rates of dissolution were determined by the change in horizontal step location between the first data point at the bottom of the image to the final data point at the top. The etching rates sped up with increasing tip normal force.

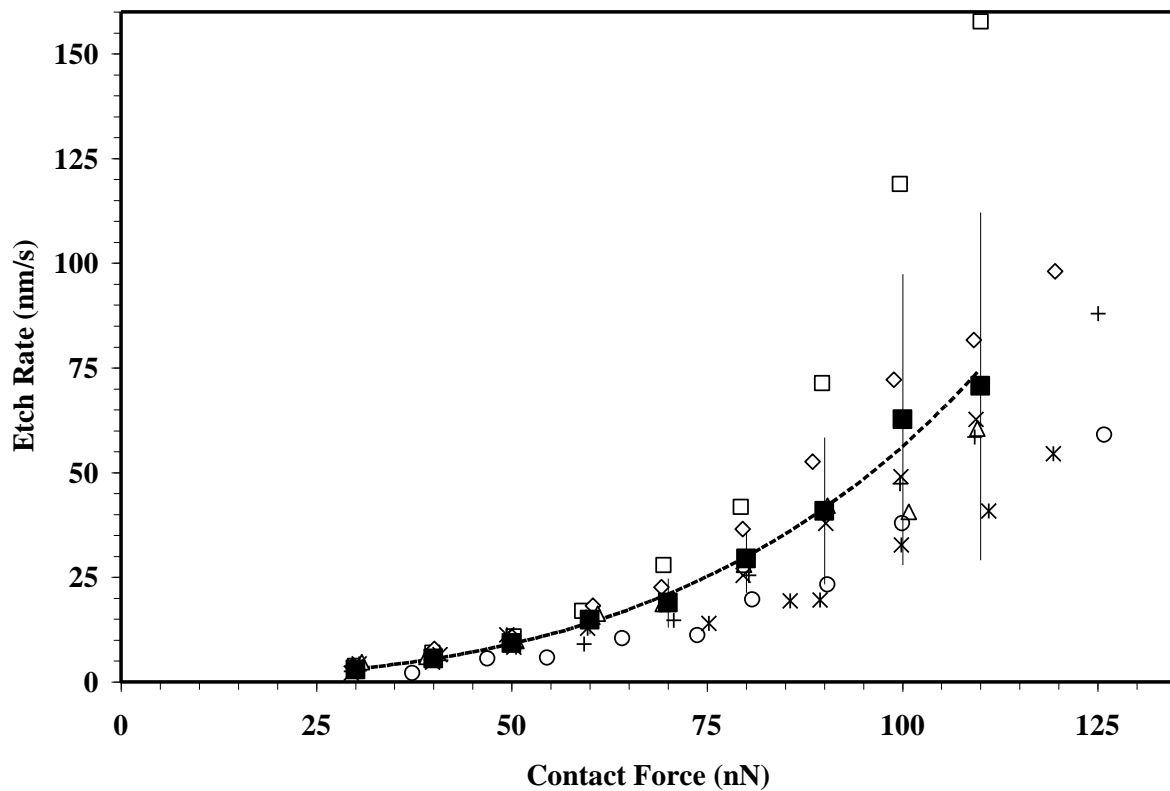
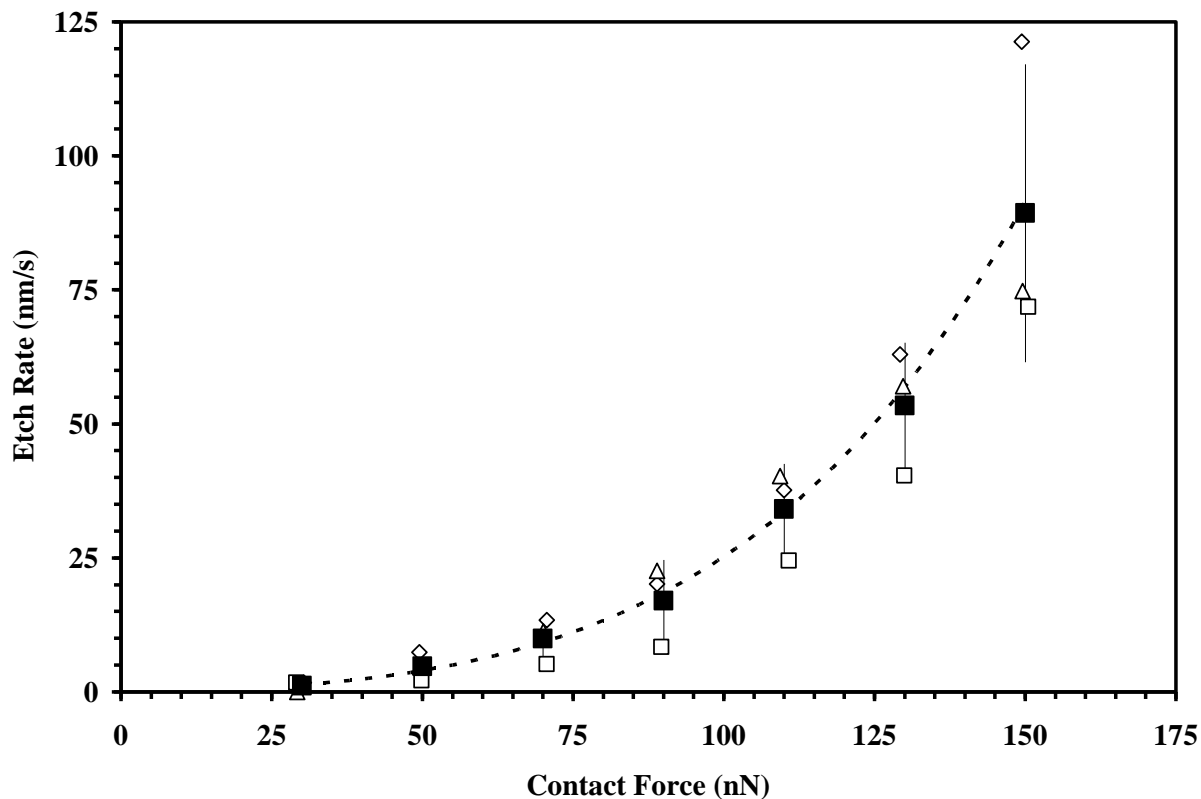
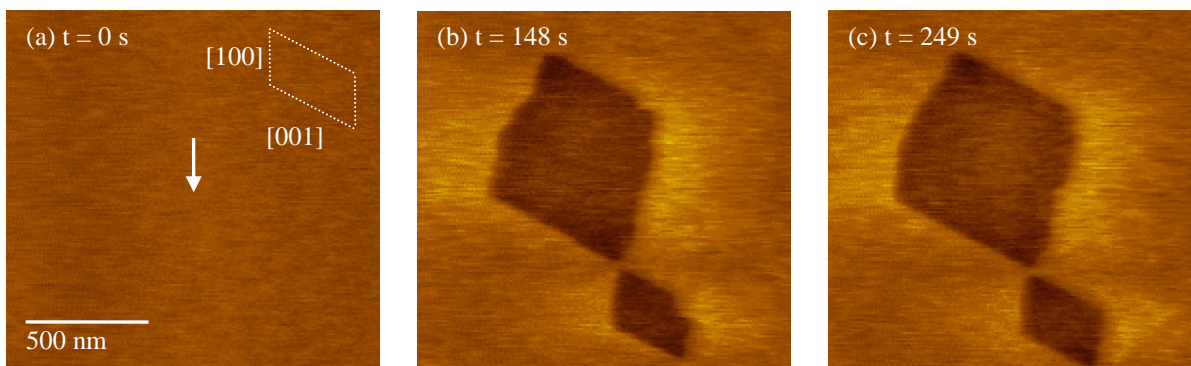


Figure 9. Etch rates are plotted versus tip normal force for linear etching performed perpendicularly to the [001] step in supersaturated solution ( $\sigma = 0.24$ ). Data from each individual experiment have identical markers. The bold squares (■) represent the averages of seven data sets, and the error bars correspond to a single standard deviation from the mean. The dashed line represents a least squares fit of the averages to the Zhurkov–Arrhenius expression given in equation [5] within the Results and Discussion.



*Figure 10.* Etch rates are plotted versus tip normal force for linear etching performed perpendicularly to the [100] step in supersaturated solution ( $\sigma = 0.46$ ). Data from each individual experiment have identical markers. The bold squares (■) represent the averages of seven data sets, and the error bars correspond to a single standard deviation from the mean. The dashed line represents a least squares fit of the averages to the Zhurkov–Arrhenius expression given in equation [5] within the Results and Discussion.



*Figure 11.* This sequence shows tip induced monolayer pit formation in supersaturated solution ( $\sigma = 0.46$ ). At  $t = 0$  seconds the tip was pressed into the (010) surface for 10 seconds at the center of image (a), as denoted by the white arrow, and with a normal force of approximately 270 nN. Image (b) was captured following indentation, showing the nucleation of two monolayer pits. No pits were observed except for in the immediate vicinity of the tip indentation location. Significant dissolution at the boundaries of the pits was not observed following the capture of image (c).

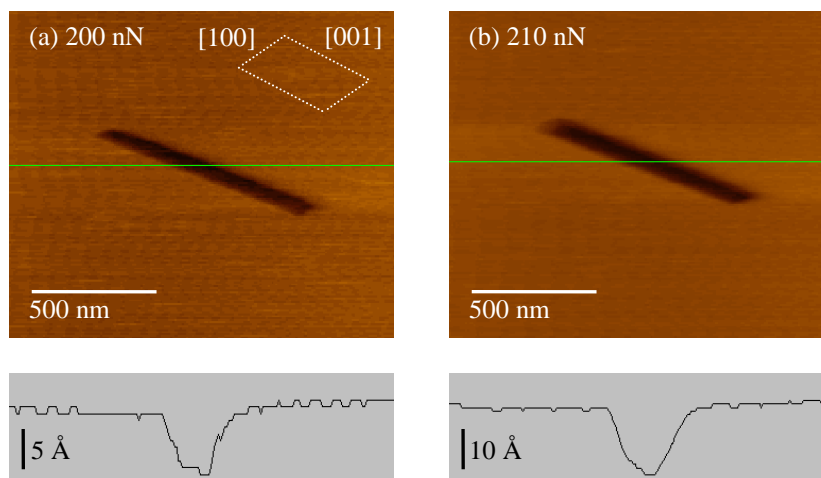


*Figure 12.* The pits formed in images (a) and (b) were from two related but unique indentation experiments in slightly undersaturated solution ( $\sigma = -0.013$ ). The SFM tip was pressed into the (010) face at the center of each image for a 1 second duration at the normal forces noted in the images. Dissolution proceeded much faster in the undersaturated solution and both pits

expanded parallel to the crystallographic  $c$  direction immediately following the indentation.

Cross-sectional data corresponding to the green lines, and shown below the images, shows that the pit in (a) is a single atomic layer in depth, while the pit in (b) is approximately two or three atomic layers deep.

## VIII. References

- 1 *Gypsum*, Wikipedia, Updated: 27 January 2008, Accessed: 28 January 2008  
<<http://en.wikipedia.org/wiki/Gypsum>>.
- 2 Edmund Baeuerlein, *Biomineralization: progress in biology, molecular biology and application*, 2nd completely rev. and extended ed. (Wiley-VCH, Weinheim, 2004).
- 3 Dirk Bosbach, Jodi L. Junta-Rosso, Udo Becker et al., *Geochimica et Cosmochimica Acta* **60** (17), 3295 (1996).
- 4 Stephen Mann, *Biomineralization: principles and concepts in bioinorganic materials chemistry*. (Oxford University Press, New York, 2001).
- 5 James J. De Yoreo and Peter G. Vekilov, in *Biomineralization*, edited by Patricia M. Dove, James J. De Yoreo, and Steve Weiner (The Mineralogical Society of America, Washington, DC, 2003), Vol. 54, pp. 381.
- 6 Dirk Bosbach, Guntram Jordan, and Werner Rammensee, *European Journal of Mineralogy* **7**, 267 (1995).
- 7 Dirk Bosbach and Werner Rammensee, *Geochimica et Cosmochimica Acta* **58** (2), 843 (1994).
- 8 J. M. Astilleros, C. M. Pina, L. Fernandez-Diaz et al., *Chemical Geology* **225**, 322 (2006).
- 9 Christopher Hall and David C. Cullen, *AIChE Journal* **42** (1), 232 (1996).
- 10 M. R. Christofferson, J. Christofferson, M. P. C. Weijnen et al., *Journal of Crystal Growth* **58**, 585 (1982).
- 11 M. P. C. Weijnen, G. M. van Rosmalen, and P. Bennema, *Journal of Crystal Growth* **82**, 528 (1987); M. P. C. Weijnen, G. M. van Rosmalen, P. Bennema et al., *Journal of Crystal Growth* **82**, 509 (1987).
- 12 N.-S. Park, M.-W. Kim, S. C. Langford et al., *Journal of Applied Physics* **80** (5), 2680 (1996).
- 13 L. Scudiero, S. C. Langford, and J. T. Dickinson, *Tribology Letters* **6**, 41 (1999).
- 14 E. Finot, E. Lesniewska, J. C. Mutin et al., *Surface Science* **384**, 201 (1997).

- 15 A. L. McEvoy, F. Stevens, S. C. Langford et al., *Langmuir* **22**, 6931 (2006).
- 16 R. Hariadi, S. C. Langford, and J. T. Dickinson, *Langmuir* **18**, 7773 (2002).
- 17 J. T. Dickinson, A. L. McEvoy, and S. C. Langford, presented at the AVS, 2005 (unpublished).
- 18 S. N. Parikh, *Journal of Postgraduate Medicine* **48**, 142 (2002).
- 19 B. F. Pederson and D. Semmingsen, *Acta Crystallographica* **B38**, 1074 (1982).
- 20 *Gypsum*, Mineral Web, Updated: Accessed: 6 Feb 2008  
<<http://www.minweb.co.uk/sulphates/gypsum.html>>; P. F. Schofield, K. S. Knight, and I. C. Stretton, *American Mineralogist* **81**, 847 (1996).
- 21 O. Knacke and W. Gans, *Zeitschrift fur Physikalische Chemie* **104** (41) (1977).
- 22 J. Christofferson and M. R. Christofferson, *Journal of Crystal Growth* **35**, 79 (1976).
- 23 S. T. Liu and G. H. Nancollas, *Journal of Inorganic and Nuclear Chemistry* **33**, 2311 (1971).
- 24 Ergun Karacan and Isik Yilmaz, *Geotechnical and Geological Engineering* **18**, 79 (2000).
- 25 Rob Lavinsky, *SeleniteClearTabularWillowCreekAlberta.jpg*, 2007, Wikipedia, Updated: 2 April 2007, Accessed: 28 January 2008,  
<<http://en.wikipedia.org/wiki/Image:SeleniteClearTabularWillowCreekAlberta.jpg>>.
- 26 Nancy and Joe Stine, *DesertRoseSaudiArabiaTimberlake.jpg*, 2007, Wikipedia, Updated: 2 April 2007, Accessed: 28 January 2008,  
<<http://en.wikipedia.org/wiki/Image:DesertRoseSaudiArabiaTimberlake.jpg>>.
- 27 Eurico Zimbres, *GipsitaEZ.jpg*, 2004, Wikipedia, Updated: 20 September 2005, Accessed: 28 January 2008, <<http://en.wikipedia.org/wiki/Image:GipsitaEZ.jpg>>.